November 28, 2025

Typeset using LaTeX **manuscript** style in AASTeX7.0.1

Asteroid Classification with Convolutional Neural Networks

Nayan Patel,[1] Thomas H. Burbine,[2] and Francesca E. DeMeo[3]

[1] *University of Pennsylvania, Philadelphia, PA 19104 USA*

[2] *Department of Physics & Astronomy, 50 College Street, Mount Holyoke College, South Hadley, MA 01075 USA*

[3] *Department of Earth, Atmospheric & Planetary Sciences, 77 Massachusetts Avenue Cambridge, Massachusetts Institute of Technology, Cambridge, MA 02139 USA*

ABSTRACT

The most widely adopted system to classify asteroids today is the Bus-DeMeo (BD) taxonomy. Currently, asteroids are sorted based on their reflectance spectra into one of twenty-five different BD classes. We have created a convolutional neural network (CNN) to automatically analyze visible and near-infrared (VISNIR) asteroid reflectance spectra and classify them into the BD taxonomy. We trained the model on a number of different asteroid spectral datasets and found that our models had accuracies from 77-84%. Our best model (84%) used a set of main-belt, Mars-crosser, and near-Earth asteroid spectra and used 80% of the set for training and 20% of testing. Overall, we demonstrate that CNNs can effectively be used to analyze asteroid spectra and can be applied to classify asteroids according to the BD taxonomy.

1. INTRODUCTION

The first letter-based asteroid taxonomy (Chapman et al. 1975) broke asteroids into three classes: S (silicaceous), C (carbonaceous), and U (unclassified) based on visible data and visual albedo. Later asteroid taxonomies based on a variety of datasets and wavelength coverages (e.g., Tholen 1984;

Email: nayanp@seas.upenn.edu, tburbine@mtholyoke.edu, fdemeo@mit.edu

Barucci et al. 1987; Bus & Binzel 2002, DeMeo et al. 2009; Carvano et al. 2010) group spectra into three main types (S-, C-, and X-types) plus a number of other classes (e.g., A, D, Q, R, V) with a variety of distinctive features and/or slopes. S-types tend to have absorption bands due to olivine and pyroxene and tend to be linked to the ordinary chondrite meteorites. C-types tend to have much much more subtle absorption bands and tend to be linked with the carbonaceous chondrites. X-types tend to have relatively flat spectra with a variety of spectral slopes and have been linked to a variety of compositions depending on visual albedo (low-albedo, organic-rich; intermediate-albedo, metallic iron; high-albedo, enstatite).

The Bus-DeMeo (BD) taxonomy (DeMeo et al. 2009) is one of the most widely used systems for classifying asteroids. The BD taxonomy currently groups asteroids into twenty-five separate classes (**Figure 1**) due to differences in the presence and strengths of absorption bands and spectral slope in the visible and near-infrared. The BD taxonomy is an extension of the Bus & Binzel (2002) taxonomy into the near-infrared while the Bus & Binzel (2002) taxonomy was an extension of the Tholen (1984) taxonomy to charge-coupled device (CCD) spectra. The Tholen (1984) taxonomy classified Eight Color Asteroid Survey (ECAS) data from 0.3-1.0 µm while the Bus & Binzel (2002) taxonomy classified CCD spectra from 0.4-0.9 µm. The significance of using near-infrared data is that both low-Ca pyroxene absorption bands can be covered with longer wavelength coverage.

To apply the BD taxonomy, both a web-based and a UNIX program were developed by Stephen Slivan to classify a spectrum using principal component scores and the spectral slope; however, visual inspection was necessary to distinguish some spectral types. Visual inspection is needed for spectra with subtle (weak) absorption bands. For meteorites, approximately 40% of all spectra needed visual inspection (Burbine et al. 2024). As noted by Burbine et al. (2024) visual inspection leads to some uncertainty in the classification for many spectra.

To try to better identify weak features in the spectra and remove the ambiguity of visual inspection in classification, we have used machine learning to classify asteroids using the BD taxonomy. Machine learning is a class of artificial intelligence models that are trained on a set of data with known results and then applied to some unknown data. Machine learning has been used previously to classify

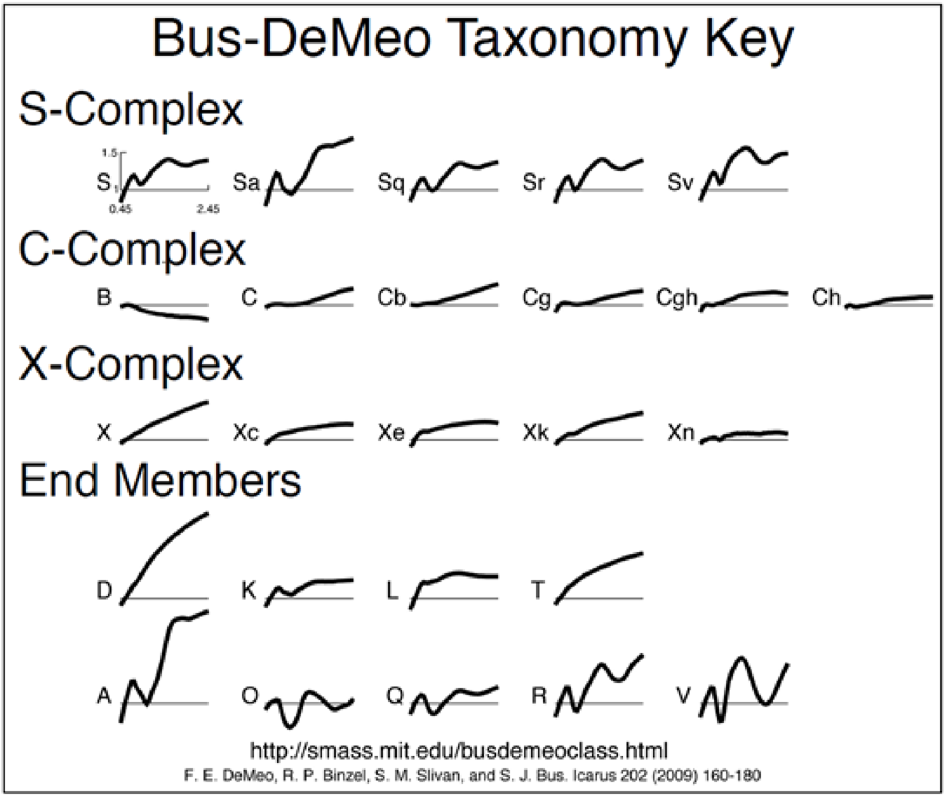

Figure 1. The Bus-DeMeo taxonomy key (DeMeo et al. 2015) displays reflectance spectra of each of the taxonomic classes. The wavelength range of each spectrum is 0.45 to 2.45 µm.

asteroids from photometry taken by large sky surveys (e.g., Penttilä et al. 2021; Klimczak et al. 2022; Sullivan 2023; Ge et al. 2024). Mahlke et al. (2022) used machine learning to classify both partial and complete observations in the visible and/or near-infrared and also incorporated visual albedo in the classification. Ojeda et al. (2025) expanded on this work and investigated the significance of missing data and visual albedo on applying machine learning algorithms to visible and near-infrared spectra. Machine learning has also been trained on meteorite spectra to try to mineralogically classify asteroid spectra (Dyar et al. 2023; Saha et al. 2025; Nath et al. 2025).

To see how well machine learning can classify asteroid spectra, we applied a machine learning algorithm to three sets of asteroid spectra, all taken from a pool of 627 asteroids from two publicly available datasets: DeMeo et al. (2009) and Binzel et al. (2019). Each run varied the input to include a mix of main-belt, near-Earth, and Mars-crossing asteroids.

2. DATA

Our initial training dataset consisted of the spectra that were used to define the BD taxonomy (DeMeo et al. 2009), which primarily contained main-belt asteroid spectra. We also included four Xn spectra from the Binzel et al. (2019) study of near-Earth asteroids (NEAs) and Mars-crossers called MITHNEOS (MIT-Hawaii Near-Earth Object Spectroscopic Survey). Our initial testing dataset was the Binzel et al. (2019) spectra of NEAs and Mars-crossers after excluding any objects used in defining the BD taxonomy and the 4 Xn spectra (leaving 1 remaining Xn spectrum) used for training. Our second training dataset was composed of DeMeo et al. (2009) spectra plus NEAs from Binzel et al. (2019) spectra. Our second testing dataset was Mars-crossers, which would be expected to have sizes intermediate between main-belt and NEAs. Our third training dataset was a random 80% of all the reflectance spectra (main-belt, Mars-crossers, NEAs). Our third testing dataset was the 20% of the reflectance spectra that were not part of the training set. The distribution of the classes for each training run are given in **Table 1** and the distribution of asteroid classes for each testing run are given in **Table 2**. Prediction accuracies for each class for each run are also listed in **Table 2**. Testing results for particular asteroids are given in **Appendix A**.

Table 1. Distribution of asteroid classes for the training spectra for the three runs.

Class	Run 1	Run 2	Run 3
A	6	6	6
B	4	5	10
C	13	26	25
Cb	3	3	3
Cg	1	1	1

Table 1 *continued on next page*

Table 1 *(continued)*

Class	Run 1	Run 2	Run 3
Cgh	10	9	8
Ch	18	18	15
D	16	18	18
K	16	14	13
L	22	31	28
O	1	1	1
Q	8	20	36
R	1	1	1
S	144	144	174
Sa	2	1	2
Sq	29	33	51
Sr	22	23	34
Sv	2	2	4
T	4	3	3
V	17	20	23
X	4	13	13
Xc	3	3	3
Xe	7	6	9
Xk	18	18	18
Xn	4	1	1
Total	375	420	500

Table 2. Distribution (#) of asteroid classes for the test spectra for the three runs and percentage of correct predictions (Acc).

	Run 1		Run 2		Run 3	
Class	#	Acc	#	Acc	#	Acc
A	1	100%	1	100%	1	100%
B	7	86%	7	57%	2	50%
C	16	56%	5	100%	6	100%
Cb	1	100%	1	100%	1	100%
Cg	1	0%	1	0%	1	0%
Cgh	0	-	1	100%	2	50%
Ch	2	50%	1	100%	4	100%
D	6	67%	4	100%	4	100%
K	0	-	2	100%	3	100%
L	12	58%	4	50%	7	100%
O	0	-	1	100%	1	100%
Q	37	76%	25	60%	9	100%
R	0	-	1	100%	1	100%
S	73	88%	74	84%	44	86%
Sa	1	100%	2	100%	1	100%
Sq	31	97%	31	84%	13	77%
Sr	18	89%	19	79%	8	63%
Sv	3	67%	3	33%	1	0%
T	0	-	1	100%	1	0%
V	12	100%	9	100%	6	100%

Table 2 *continued on next page*

Table 2 *(continued)*

	Run 1		Run 2		Run 3	
Class	#	Acc	#	Acc	#	Acc
X	13	31%	3	100%	3	100%
Xc	1	0%	1	0%	1	0%
Xe	4	25%	5	60%	2	50%
Xk	4	25%	4	75%	4	75%
Xn	1	0%	1	100%	1	0%
Total	244	77.0%	207	79.2%	127	83.5%

The DeMeo et al. (2009) dataset included 371 asteroid spectra measured from 0.45 to 2.45 µm with increments of 0.0025 µm and normalized to unity at 0.55 µm. It consists primarily of main-belt objects. The visible spectra were primarily taken from the Small Main Belt Asteroid Spectroscopic Survey (SMASS II) dataset (Bus & Binzel, 2002) of CCD observations taken at Kitt Peak while the near-infrared spectra were taken at the NASA Infrared Telescope Facility observations on Mauna Kea. The Binzel et al. (2019) dataset included both Mars-crossers and NEAs and included both reflectance spectra and color photometry over a wide range of wavelengths since the spectra were compiled from a variety of sources. The Binzel et al. (2019) near-infrared spectra were primarily taken at the IRTF. We used the Binzel et al. (2019) data that had the full visible and near-infrared wavelength range (0.45-2.45 µm) consistent with the DeMeo et al. (2009) spectra. All spectra were fit to be at the same wavelengths as the DeMeo et al. (2009) data. Data from Binzel et al. (2019) that covered only the near-infrared range (0.8-2.45 µm) were excluded. For the same reason, later survey data from Marsset et al. (2022), which were also predominantly limited to the near-infrared, were excluded.

To prepare the data for training, each spectrum was plotted on a graph with a standardized x axis from 0.45-2.45 µm. The range of each graph was 0.8 reflectance units, centered around the mean of the reflectance values for each graph. Each graph was then converted to grayscale and resized to 128x128 pixels, enabling their direct use as inputs to our convolutional neural network, which requires image-based data.

3. METHODS

We used convolutional neural networks (CNNs) to classify the asteroid spectra. CNNs are a type of machine learning model particularly well suited to analyzing images and extracting local features through convolution via their strengths in locality and invariance. This pattern recognition helps CNNs excel in classification tasks where similar features must be grouped together, which is why a CNN was chosen for this task. The premise of convolution is taking an $k \times k$ filter matrix K and sliding it over an $k \times k$ area of the input matrix I, computing the dot product and entering the resulting value into an output matrix O.

$$O(i,j) = \sum_{m=0}^{k-1} \sum_{n=0}^{k-1} (I(i+m),(j+n)) \cdot K(m,n) \tag{1}$$

Where (i, j) is the position of the output matrix. We can apply this matrix operation to an image, with input matrix I being the input image filled with pixels, filter matrix K filled with adjustable weights, and the output matrix O being the resulting convolution. We can adjust the values (weights) in the filter matrix K to change the features extracted in the output matrix O, ultimately changing the model's final prediction. We can then use loss functions to optimize the weights and maximize the success of the model's predictions.

Our CNN (**Figure 2**) was built in PyTorch (a machine learning library) to receive and classify asteroid spectra. The model featured three 2-D convolution layers, each with a kernel size of 3, stride of 1, and padding of 1. In between each convolution was a maxpool layer with a kernel size of 2. A maxpool layer reduces the dimensionality of the input by taking the maximum value in each kernel-sized section of the input. This helps to reduce overfitting and improve computational efficiency.

Each convolutional layer was followed by a ReLU (rectified linear unit) activation function, which introduces non-linearity to the model and helps it learn complex patterns in the data.

After the 2-D features are extracted, the image is flattened and fed into a linear (aka. fully-connected or dense) layer, classifying the features into one of the 25 BD classes. The model was trained using the Adam optimizer with a learning rate of 0.001 and a cross-entropy loss function.

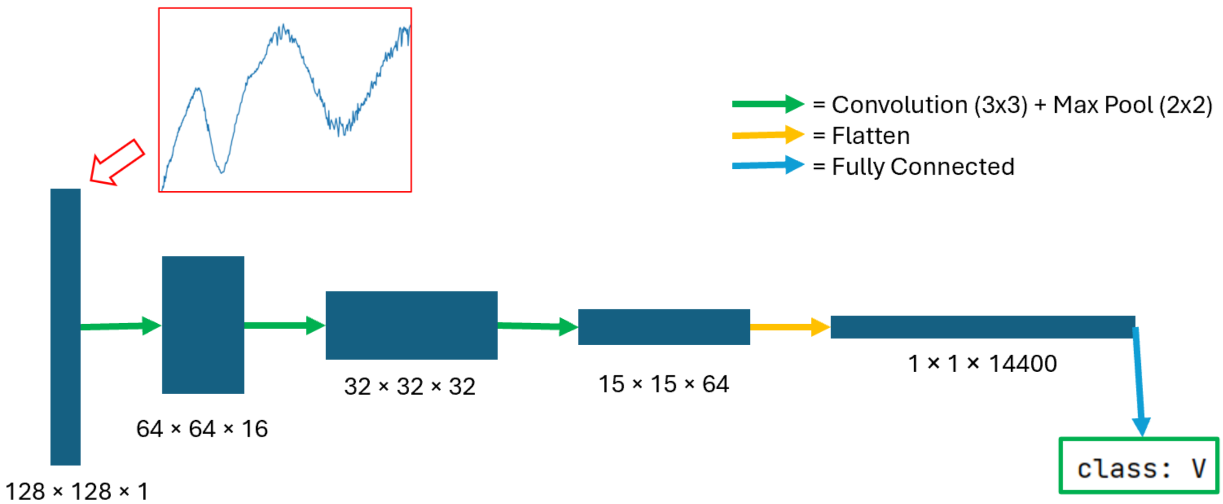

Figure 2. Map of the CNN architecture. The example shows the process for classifying an asteroid as a V-type.

We opted to use three different combinations of training/testing data, labeled Run 1, Run 2, and Run 3. Each run separates asteroids into a training set and a testing set based on various asteroid characteristics (main-belt, near-Earth, or Mars-crosser) that may impact an asteroid's spectral type due to size or orbit. We aim to determine if grouping these asteroids in certain ways improves or detracts from model performance.

3.1. *Run 1*

Our initial training data was sourced from data used by DeMeo et al. (2009). Reflectance spectra for the newer Xn asteroid class was sourced from Binzel et al. (2019), resulting in 375 total training spectra (**Table 1**).

Our initial testing data was sourced from the Binzel, et al. (2019) study of near-Earth and Mars-crossing asteroids. The data was filtered to only include VISNIR data from 0.45-2.45 µm. All spectra in the test dataset that are duplicates of an asteroid in the training dataset were removed, leaving 244 spectra for testing.

The model was trained with the 375 asteroid spectra with an 80/20 train/validation split for 20 epochs. To test the model's performance, 244 VISNIR spectra were compiled from Binzel, et al. (2019). Asteroids within the Binzel, et al. (2019) dataset that overlapped with asteroids in the training dataset were not used for testing.

3.2. *Run 2*

To expand the training set, we combined data from DeMeo et al. (2009) and Binzel et al. (2019) to create a single set of 627 asteroid spectra. Next, we removed the Mars-crossers from the set and used them to test the model, leaving only NEAs and main-belt asteroids for training. Our logic was that NEAs tend to be relatively small while main-belt asteroids are generally much larger, allowing for spectra of a large range in asteroid sizes to be used for training. Since Mars-crossers tend to be slightly larger than NEAs and are transitioning from main-belt to NEA orbits, they would offer a more diverse testing set. The distribution of test spectra by class is shown in **Table 2**. For classes without Mars-crossers, (Cg, Cgh, O, R, T) a random asteroid spectrum for those classes from the training set was chosen for testing. The Cg, O, and R classes only contain a single asteroid, so those asteroid spectra were copied over to the testing set to provide metrics.

After training for 20 epochs on the 420 non-Mars-crosser spectra, the model was evaluated on the 202 Mars-crossers, plus five extra spectra from the Cg, Cgh, O, R, and T classes (207 total spectra).

3.3. *Run 3*

The final way we evaluated our model was by splitting the combined 627 asteroid dataset into two smaller ones without separating based on any asteroid attribute. 80% of the asteroids in each class were randomly selected to be used in the training set, while the remaining 20% were set aside for testing.

If the class had less than five asteroids, one asteroid was used for testing. If the class only had one asteroid, the single asteroid was duplicated into the testing set. This resulted in a final training dataset of 500 asteroids and a testing dataset of 127 asteroids.

4. RESULTS

4.1. *Run 1*

The model's performance for each class is shown below in the confusion matrix (**Figure 3**). We note that some asteroids were classified by Binzel et al. (2019) with multiple classifications. For asteroids where this is the case, it is only counted as an "occurrence" under the type that the model guessed correctly. If the model predicted the class of an asteroid with multiple classifications incorrectly (predicted neither class), the asteroid is counted under the class with less total asteroids.

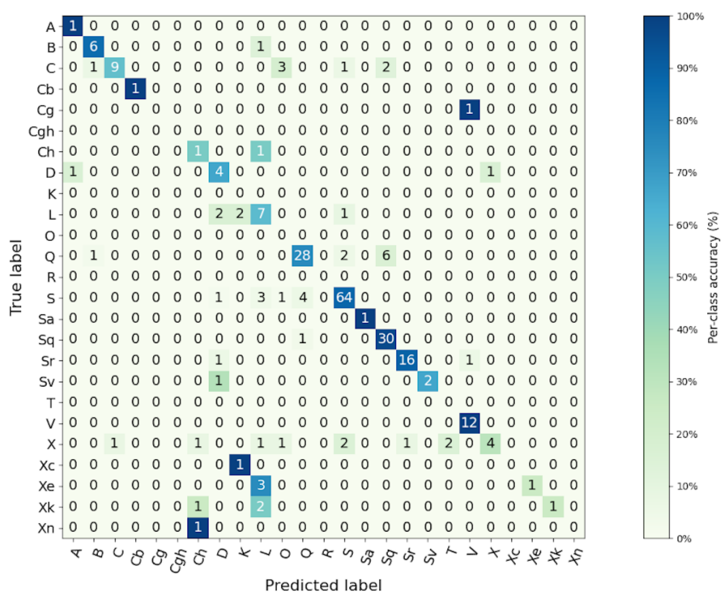

Figure 3. Confusion matrix for Run 1, trained on 371 asteroids from DeMeo et al. (2009) plus 4 Xn-types from Binzel et al. (2019) and tested on NEA and Mars-crosser spectra from Binzel et al. (2019). Darker blue colors indicate a higher number of objects in the correct bin.

A confusion matrix plots the number of accurately predicted classes versus the true classes for the asteroids. Diagonal values show the number of correct predictions for each class, while off-diagonal values show misclassifications. A perfect classification system will have all the numbers on the diagonal stretching from top left to bottom right, meaning that all the predicted classes agree with the true classes. As the classification percentage worsens, more predicted classes will deviate from the true classes and more numbers will be listed off the diagonal.

Our accuracy for Run 1 was 77.05%. We list in **Table 2** the prediction percentage for each class for Run 1 and list in **Appendix A** the predictions for individual asteroids in the test sample. For classes with a relatively large number of test samples, Sr- (89%), S- (88%), and V-types (100%) had high accuracies. These asteroid types tend to have relatively strong absorption bands (**Figure 1**). The Sr- (22 spectra), S- (144), and V-types (17) also had a relatively large number of spectra in the training set, which allowed the spectral diversity in each class to be characterized in the training. Q-types (76%) have lower accuracies and a wide variety of mismatches (e.g., B, S, Sq) (**Figure 3**), which could be potentially due to Q-types having a relatively small number (8) in the training dataset. X-types (31%) also have a low percentage and this could be due to also having a relatively small number (4) in the training set.

Interestingly in Run 1, three C class asteroids were misclassified as O class asteroids, considering the relative rarity of the O class. We decided to look at the three C-class spectra (**Figure 4** in particular that were misclassified as O. These objects tended to have a relatively broad but weak band centered at 1.25 µm. The classification algorithm appears to be focused on the structure of the band but not its strength. For sake of comparison, refer to **Figure 5** for the spectrum of asteroid (3628) Božněmcová, a true O type asteroid.

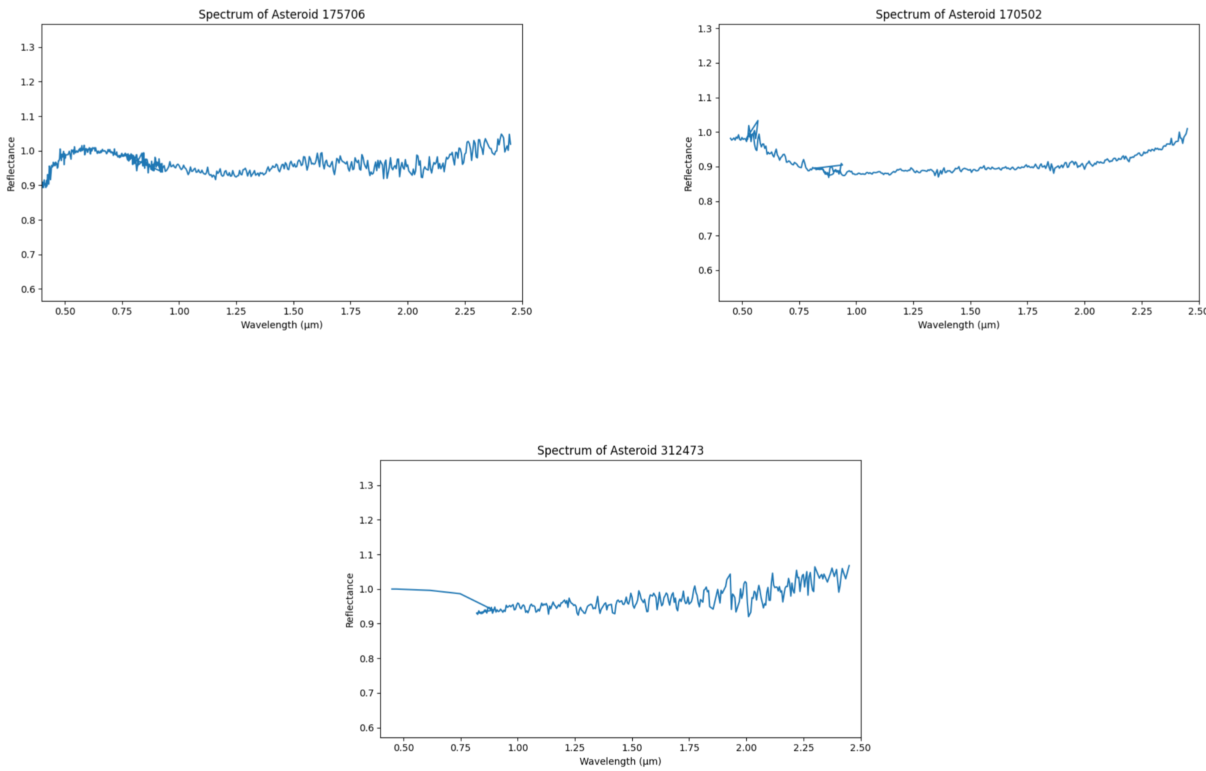

Figure 4. Reflectance spectra of three C-types that were classified as O-types in Run 1.

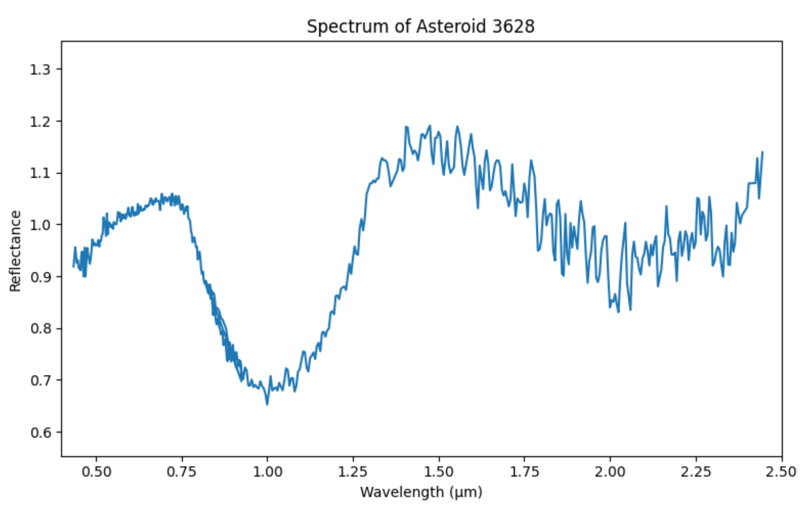

Figure 5. Spectrum of (3628) Božněmcová, an O type asteroid, for reference.

4.2. *Run 2*

After training for 20 epochs, the model achieved an accuracy of 79.23%. The confusion matrix is displayed in **Figure 6**. We list in **Table 2** the prediction percentage for each class for Run 2 and list in **Appendix A** the predictions for individual asteroids in the test sample. Similar to Run 1 for types with a relatively large number of samples to test, V- (100%), S- (84%), and Sq-types (84%) had high accuracies. However, Q-types had a lower accuracy (60%) than Run 1 even though there were more Q-types in the training dataset (20) compared to Run 1 (8).

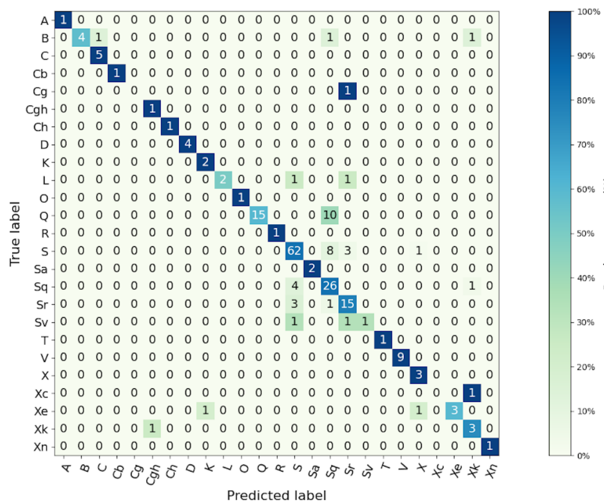

Figure 6. Confusion matrix Run 2, trained on 420 non-Mars-crossing spectra primarily from DeMeo et al. (2009) and tested on 207 Mars-crosser spectra. Darker blue colors indicate a higher number of objects in the correct bin.

4.3. *Run 3*

After training for 20 epochs, the model achieved an accuracy of 83.46% on the testing set. The confusion matrix is displayed in **Figure 7**. We list in **Table 2** the prediction percentage for each class for Run 3 and list in **Appendix A** the predictions for individual asteroids in the test sample. Similar to Runs 1 and 2 for types with a relatively large number of samples to test, V- (100%), S-

(86%), and Sq-types (77%) had high accuracies. In contrast to Runs 1 and 2, Q-types had a 100% accuracy.

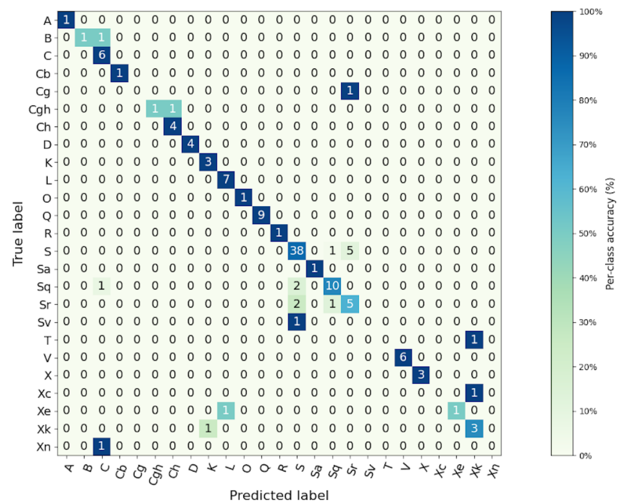

Figure 7. Confusion matrix for Run 3, trained on 500 asteroids from DeMeo et al. (2009) and Binzel et al. (2019) and tested on 127 asteroids from the same datasets. Darker blue colors indicate a higher number of objects in the correct bin.

5. DISCUSSION

5.1. *Impact of Training Set Composition on Classification Accuracy*

A compilation of all of our trials and accuracy can be found in **Table 3**. Overall, we see that the machine learning models can consistently classify asteroids reasonably accurately, with most training methods resulting in accuracy of around 80%. Run 3, which trained on a random dataset of main-belt, Mars-crossers, and NEAs had the highest accuracy. While a higher overall accuracy can be attributed to Run 3's largest training set size, we can still observe accuracy improvement in specific classes such as L and Xk, where training and test sets are drawn from a similar underlying population (main-belt objects, Mars-crossers, and NEAs). The other models have slightly lower accuracies since they train on spectra from a particular dynamical type of object and test on data from another dynamical type. Also from **Tables 1** and **2**, we see that the machine learning classification accuracy tends to be highest for classes that have more members to train on. For example, for the most abundant S class, there was 86% accuracy for Run 3, showing a clear upward trend as more data are introduced.

Table 3. A listing of the training and test datasets with the accuracy for each run. Numbers in **bold** are the total objects in each training and test dataset, respectively.

Runs	Training Dataset	Test Dataset	Accuracy
Run 1	**375** total; 371 BD asteroids (main-belt) and 4 Xn class asteroids	**244** MITHNEOS asteroids (Mars-crossers and NEAs)	77.05%
Run 2	**420** non-Mars-crossers (main belt and NEAs)	**207** total; 203 Mars-crossers and 1 Cg, 1 Cgh, 1 O, 1 R, and 1 T	79.23%
Run 3	**500** random asteroids (80% of the total dataset)	**127** random asteroids (remaining 20%)	83.46%

The boundaries between asteroid classes in traditional taxonomies (e.g., DeMeo et al. 2009) are sharply defined, but they are imposed on spectral properties that in reality vary along a continuum. For example, the division between Q-types and Sq-types is inherently ambiguous, as spectra on either side of this boundary can appear very similar. Consequently, some of the discrepancies between the predicted labels in this study and the "true" labels may reflect differences in where the boundary is drawn, rather than genuine misclassifications.

There are several concrete examples of such boundary-related discrepancies in our results. In Run 1, X-types were distributed across a wide range of predicted labels—including X, T, C, Ch, L, and S. With the exception of the S-types, these assignments can largely be explained by overlaps among adjacent spectral classes. Also in Run 1, most Q-types were correctly identified (28 as Q), but a small fraction were classified as S (2) or Sq (6). The latter is unsurprising given the close boundary between Q and Sq, whereas the few assigned to S likely reflect the influence of more distant boundary differences. Similarly, L-types in the DeMeo et al. (2009) taxonomy span a relatively broad range of characteristics, so their dispersion across multiple predicted classes is not unexpected.

The most striking example, however, comes from Run 2. Here, 15 Q-types were predicted as Q while 10 were predicted as Sq, suggesting that the CNN drew the Q/Sq boundary in a different location than the PCA-based taxonomy. This pattern underscores the possibility that machine learning models may, in some cases, be identifying alternative boundary placements.

6. CONCLUSIONS

Machine learning algorithms appear to be a very useful tool for classifying asteroid reflectance spectra with classification accuracies between 77-84%. The best classification accuracy is for the run that used a random sample of asteroids for a variety of sizes and orbits that included main-belt objects, Mars-crossers, and NEAs.

Additionally, our results highlight that discrepancies between predicted and "true" labels often arise near taxonomic boundaries, where spectra vary along a continuum. In such cases, the convolutional neural network may be identifying alternative placements of boundaries that are equally plausible.

ACKNOWLEDGMENTS

THB would like to thank the Remote, In Situ, and Synchrotron Studies for Science and Exploration 2 (RISE2) Solar System Exploration Research Virtual Institute (SSERVI) (NASA grant 80NSSC19M0215) for support. All (or part) of the data utilized in this publication were obtained and made available by the MITHNEOS MIT-Hawaii Near-Earth Object Spectroscopic Survey. The IRTF is operated by the University of Hawaii under contract 80HQTR24DA010 with the National Aeronautics and Space Administration. The MIT component of this work is supported by NASA grant 80NSSC22K0773.

APPENDIX

A. TESTING RESULTS FOR INDIVIDUAL ASTEROIDS

Table A1.

Number or Designation	Class	Run 1 Prediction	Run 2 Prediction	Run 3 Prediction
4	V	-	-	V
13	Ch	-	-	Ch
17	S	-	-	S
24	C	-	-	C
28	S	-	-	S
29	S	-	-	S
34	Ch	-	-	Ch
38	Cgh	-	Cgh	-
41	Ch	-	-	Ch
...	...	...	...	...
2011WV134	S	S	-	-

NOTE—This table is published in its entirety in the machine-readable format. A portion is shown here for guidance regarding its form and content.

REFERENCES

Barucci, M. A., Capria, M. T., Coradini, A., Fulchignoni, M. 1987, Icarus, 72, 304, doi:10.1016/0019-1035(87)90177-1

Binzel, R. P., DeMeo, F. E., Turtelboom, E. V., et al. 2019, Icarus, 324, 41, doi:10.1016/j.icarus.2018.12.035

Burbine, T. H., Khanani, I., Kumawat D., et al. 2024, PSJ, 5, 194, doi:10.3847/PSJ/ad57b6

Bus, S. J. & Binzel, R. P. 2002, Icarus, 158, 106, doi:10.1006/icar.2002.6856

Carvano, J. M., Hasselmann, P. H., Lazzaro, D., Mothé-Diniz, T. 2010, A&A, 510, A43, doi:10.1051/0004-6361/200913322

Chapman, C. R., Morrison, D., Zellner, B. 1975, Icarus, 25, 104, doi:10.1016/0019-1035(75)90191-8

DeMeo, F. E., Binzel, R. P., Slivan, S. M., & Bus, S. J. 2009, Icarus, 202, 160, doi:10.1016/j.icarus.2009.02.005

Dyar, M. D., Wallace, S. M., Burbine, T. H., et al. 2023, Icarus, 406, 115718, doi:10.1016/j.icarus.2023.115718

Ge, J., Zhang, X., Li, J., et al. 2024, A&A, 692, A100, doi:10.1051/0004-6361/202451971

Klimczak, H., Oszkiewicz, D., Carry, B., et al. 2022, A&A, 667, A10, doi:10.1051/0004-6361/202243889

Mahlke, M., Carry, B., and Mattei, P.-A. 2022, A&A, 665, A26, doi:10.1051/0004-6361/202243587

Ojeda, A. V., Guerrero, C. A., Tapia, J. J., Sánchez, L. H. 2025, JATIS, 11, 028006, doi:10.1117/1.JATIS.11.2.028006

Nath, R., Mali, S., Denesh, K., et al. 2025, M&PS, 60, 1063, doi:10.1111/maps.14342

Penttilä, A., Hietala, H., and Muinonen, K. 2021, A&A, 649, A46, doi:10.1051/0004-6361/202038545

Saha, S., Burbine, T. H., & Dyar, M. D. 2025, LPSC, 56, 2081

Sullivan, P. 2023. PhD thesis, Liverpool John Moores University, doi:10.24377/LJMU.t.00021526